Journal of Colloid and Interface Science 509 (2018) 94–101

Contents lists available at ScienceDirect

Journal of Colloid and Interface Science

journal homepage: www.elsevier.com/locate/jcis

Regular Article

Global strain field mapping of a particle-laden interface using digital image correlation

S.R. Vora [a], B. Bognet [b], H.S. Patanwala [b], C.D. Young [a], S.-Y. Chang [b], V. Daux [b], A.W.K. Ma [a,b,*]

[a] Department of Chemical and Biomolecular Engineering, University of Connecticut, Storrs, CT 06269, United States
[b] Polymer Program, Institute of Materials Science, University of Connecticut, Storrs, CT 06269, United States

GRAPHICAL ABSTRACT

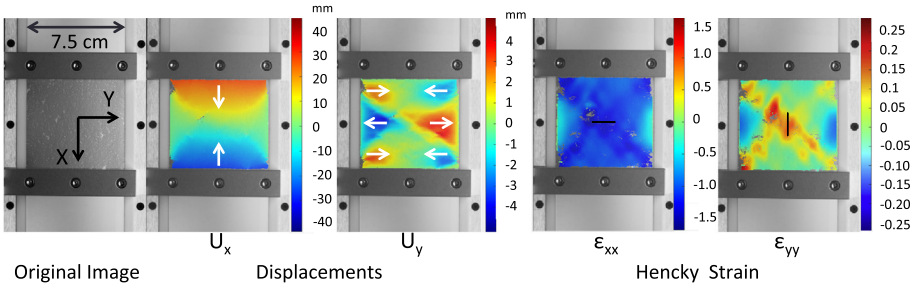

ARTICLE INFO

Article history:
Received 15 May 2017
Revised 24 August 2017
Accepted 24 August 2017
Available online 1 September 2017

Keywords:
Interfacial rheology
Surface pressure – area isotherms
Digital image correlation
Langmuir trough

ABSTRACT

Hypothesis: The ability to identify the stress-strain relations correctly is critical to understanding and modeling any rheological responses of an interface. Langmuir-Pockels (LP) trough is one of the most commonly used tools for studying an interface. Most, if not all, existing studies assume a 1D uniaxial compression during a LP-trough compression experiment. It is hypothesized that the deformation field is far more complex than what is typically assumed.

Experiments: To examine this hypothesis, we custom-built a glass-bottomed LP trough equipped with a camera to capture a series of optical images as a carbon nanotube (CNT)-laden interface is compressed. A digital image correlation (DIC) technique was then applied to the images to evaluate the global strain field during compression of the CNT laden interface. The DIC-corrected strain data were subsequently analyzed with the surface stress data to quantify the surface shear and dilatational moduli of the CNT-laden interface.

Findings: Our experimental findings clearly show, for the first time, the development of a non-uniform and complex 2D strain field during compression. The local strains were further quantified and compared with the usual assumption of 1D uniaxial compression. Although the compressive strain averaged over the whole trough area closely resembles the 1D uniaxial compression strain, the 1D compression assumption underestimates the local strain by about 36% at the center of the trough, where the surface stresses are measured. This is the first study in applying the DIC technique to map out the global strain field as a particle-laden interface is compressed. The method may also be applicable to other systems with similar optical texture, allowing the correct identification of stress-strain relationship of an interface.

1. Introduction

Langmuir-Pockels (LP) trough is one of the most common tools used for studying fluid-fluid interfaces as an interface is being

* Corresponding author at: Polymer Program, Institute of Materials Science, University of Connecticut, Storrs, CT 06269, United States.
E-mail address: anson.ma@uconn.edu (A.W.K. Ma).

http://dx.doi.org/10.1016/j.jcis.2017.08.082
0021-9797/

compressed [1]. LP trough is usually used in conjunction with a Wilhelmy plate to measure surface pressure, which is defined as the surface tension difference between a reference "clean" interface and an interface laden with soluble or insoluble components [2,3]. The surface tension is calculated by measuring the wetting force and applying a force balance in the vertical direction. It is more appropriate to treat the as-measured surface pressure as the *total surface stresses* containing contributions from both surface energies, which is subject to change due to interfacial area replaced by molecules or particles, and any rheological responses from the interface [4]. The latter are extra, or deviatoric, stresses induced by the deformation of the interface and may be viscoelastic in nature. In many cases, especially particle-laden interfaces, the rheological responses overwhelm the surface energy contributions [5–7]. Decoupling the surface energy and rheological contributions is challenging and remains an active area of research [8]. To truly understand the surface rheological responses, one needs to identify the surface stress-strain relations correctly. While the surface dilatational and shear moduli can be deduced from separate experiments by placing the Wilhelmy plate parallel and perpendicular to the barriers [9], the actual strain field is much less studied. Additionally, since the surface stresses are measured locally using a Wilhelmy plate, it is imperative to measure the corresponding local strain to capture the true stress-strain relations. Almost all existing studies assume purely uniaxial compression at the trough center as the barriers move closer together. This assumption is valid if there is perfect slip at the side edges of the trough or if the trough is sufficiently wide.

The goal of this work is to examine this long-held and widely used assumption. Earlier attempts have been made by Malcolm et al. and Aumaitre et al. Theses authors deposited sulfur particle lines onto a protein-laden surface to study the local strain field near the deposited lines [10,11]. Their findings suggest the presence of friction at the wall leading to a decaying strain field towards the trough side edges. In this study, the complete global strain field during a LP trough compression experiment is mapped out, for the very first time, using digital image correlation (DIC). Unlike previous studies, this study takes advantage of the intrinsic optical texture of a carbon nanotube-laden interface and does not require the deposition of foreign particles, which may modify the strain field. The method reported herein may be applied to other experimental systems with similar optical texture. This will further allow the correct identification of true surface stress–strain relations—the basis upon which any interfacial constitutive models are developed.

2. Experimental method

2.1. Materials and imaging setup

Carbon nanotubes (CNTs) used in this study were produced using chemical vapor deposition method (Sigma Aldrich; Cat# 659258, Lot# MKBG9911V). They were used without any further purification or chemical treatment. The D-band to G-band ratio of the Raman spectrum for the CNTs is ~0.17, suggesting that the CNTs are relatively free of defects [12] (Supporting Information, Fig. S1). The CNTs have an average diameter and length of 128 nm and 2.5 μm, respectively. Detailed length and diameter distribution data are included in Supporting Information (Fig. S2). The CNT dispersions were prepared by sonicating dry CNT powders in chloroform using a Branson 450 Digital Sonifier (2 h; 20% amplitude). An initial CNT concentration of 0.2 mg/mL was prepared and the actual concentration of the CNT dispersion was calibrated based on the optical absorbance at a wavelength of 500 nm (Shimadzu, UVmini-1240 UV–Vis spectrophotometer). Detailed procedure and calibration curve are included in the Supporting Information (Fig. S3). The CNT-chloroform dispersion was added drop-wise to an air–water interface using a 500-μL syringe until the desired CNT coverage was reached. A total CNT amount of 0.684 mg was added in all the experiments. Further details on the experimental protocol can be found in previous work [5].

A commercially available LP trough (KN 3005 LP trough; KSV Nima) was modified by replacing the actual trough with a custom-built glass-bottomed trough (Fig. 1). No modifications have been made to the microbalance or barriers. The glass bottom allows for direct visualization as the interface is being compressed. The barriers of the LP trough were compressed at an arbitrary rate of 5 mm/min for all the experiments. A Nikon Digital Single-Lens Reflex (DSLR) camera was positioned above the LP trough to capture images of the CNT-laden interface at intervals of 10 s. Optical images for DIC analysis were captured in the absence of a Wilhelmy plate and microbalance, which will otherwise obscure the field of view. The images were then used for further DIC analysis to calculate the displacements and strains of the CNT-laden interface as a function of compression area.

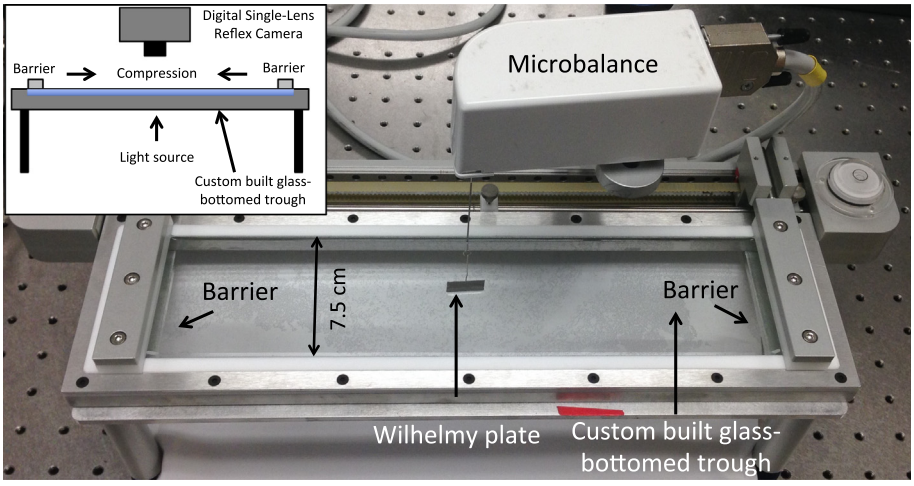

Fig. 1. Experimental setup for mapping out the global strain fields. Inset figure shows the schematic diagram. The setup is based on a commercially available Langmuir-Pockels (LP) trough (KN 3005 LP trough; KSV Nima) comprising a Wilhelmy microbalance and barriers as indicated. A custom-built glass-bottomed trough is used for direct visualization of the compression area without obstruction.

2.2. Digital image correlation (DIC) protocol

DIC is a non-contact technique widely used in solid mechanics for capturing material deformations based on optical texture or more specifically "speckle patterns" [13]. Speckle patterns are usually created by spraying paints onto a specimen non-uniformly. In this paper, DIC analysis is possible because of the intrinsic speckle-like texture of a CNT-laden interface. An open-source subset-based 2D DIC software package for MatLab called Ncorr was employed for the DIC analysis [14]. Fig. 2 shows the workflow of the DIC process as used by Ncorr. First, a reference image needs to be chosen. For our analysis, we used the image with no compression as the reference image as shown in Fig. 2a. The next step is to select and input all the images for DIC analysis. The evolution of the CNT microstructure was followed by analyzing images captured every 20 s during the course of compression. After inputting the optical images, the region of interest (ROI) was specified for further analysis. Ncorr is a subset-based 2D DIC package, where ROI is partitioned into smaller regions called "subsets". The deformation is assumed to be homogeneous within a subset. There are two user-defined parameters, namely, the subset radius (r_s), which defines the size of the subset, and the subset spacing (S), which dictates the distance between the subsets. Fig. 2c shows a preview of the speckle pattern with arbitrarily chosen values of r_s and S. Using the first image as reference, displacements are then computed by comparing the non-deformed subsets in the reference image against the deformed subsets in subsequent images (Fig. 2d). Further details on the DIC algorithms are available at: http://www.ncorr.com/index.php/dic-algorithms (accessed April 2017). Strains are calculated from the displacements after specifying another user-defined parameter called "strain radius (r_{st})". The strain radius divides the global strain field into smaller subsets having a radius r_{st} as shown in Fig. 2e. A plane is then fit through the points within each subset to yield longitudinal, lateral, and shear

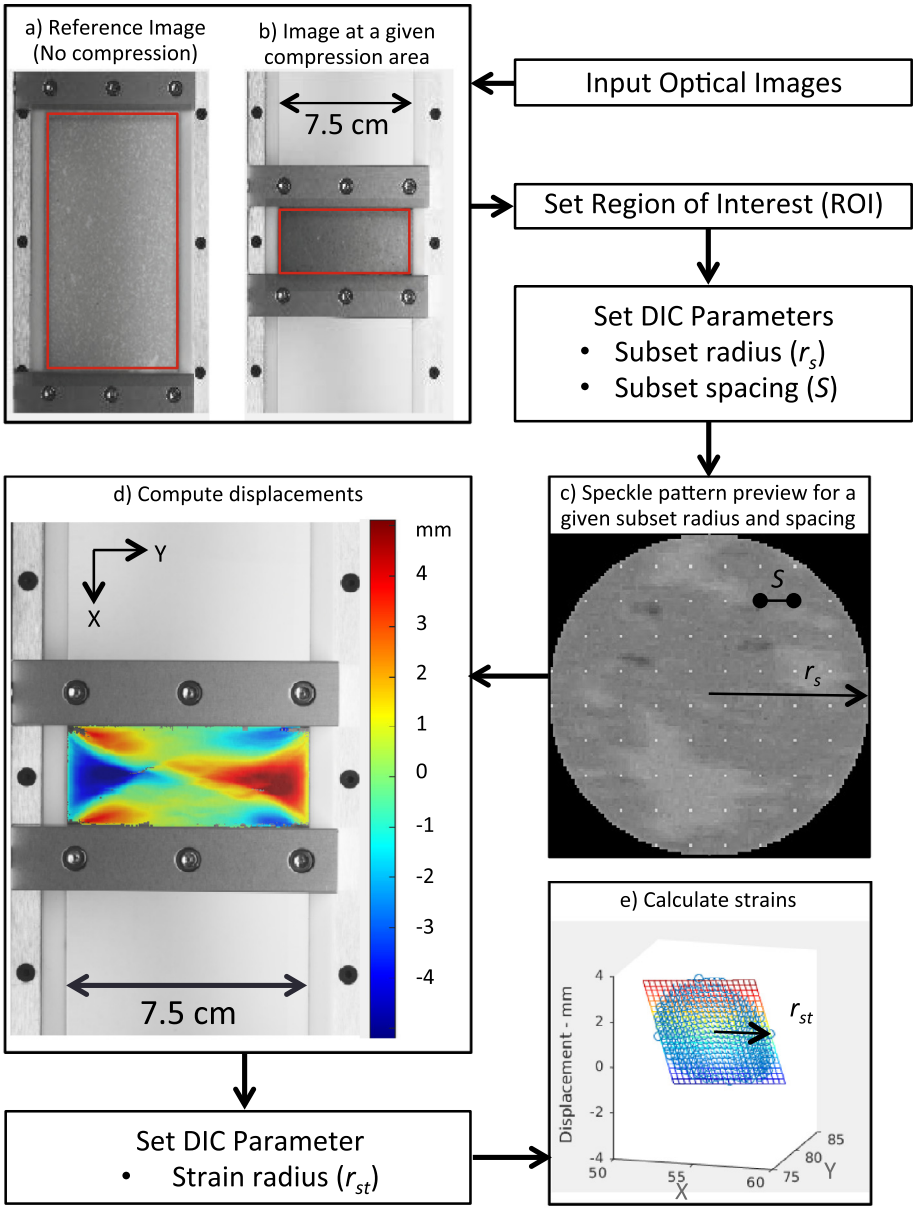

Fig. 2. Workflow of the digital image correlation (DIC) analysis used in this study: (a) is a sample reference image and (b) is a sample image captured subsequently at a given compression area. The red rectangles in (a) and (b) represent the region of interest (ROI) selected. (c) Sample speckle pattern for arbitrarily chosen values of r_s = 60 pixels and S = 12 pixels. (d) Sample displacement field perpendicular to the direction of compression and (e) strain computation from displacements.

strain values depending on the direction in which the slope is taken. Sensitivity analysis on all three user-defined parameters (i.e., r_s, S, and r_{st}) was carried out and is included in Section 3.2. In this paper, all the data are reported in Hencky strains because of the expansion-contraction symmetry and symmetric range of principal values as discussed in a previous study by Verwijlen et al. [8] The relationship between the Hencky strain and engineering strain for 1D uniaxial compression is given as:

$$\varepsilon_{xx,1D} = \ln[1 + ((A - A_0)/A_0)] \quad (1)$$

where $\varepsilon_{xx,1D}$ is the 1D Hencky strain, A is the area of the trough and A_0 is the initial area of the trough.

In Ncorr, the 2D strains calculated were Green-Lagrangian strains, which were then converted to Hencky strains using the following equations:

$$\mathbf{H} = 1/2 \ln(2\mathbf{E} + \mathbf{I}) \quad (2)$$

where **H** is the Hencky strain tensor, **E** is the Lagrangian strain tensor obtained from Ncorr analysis and **I** is the identity matrix.

3. Results and discussion

3.1. 2D strain field mapping

Fig. 3 shows the original images as well as the DIC-computed displacement and strain fields as a function of compression area. White arrows in the figures indicate displacement directions. In the compression direction, largest displacements (U_x) were observed near the center of the barriers, and U_x decreased approaching the side edges due to the non-perfect slip condition at the side edges. Strains along the compression direction (ε_{xx}) are all negative, indicative of a compressive strain, but the strains are smaller in areas closest to the side edges (lighter blue in Fig. 3b). In the transverse direction (y), the displacement and strain fields are more complex. At the center of the trough, CNTs moved towards the side edges during compression. However, CNTs could not escape the side edges, resulting in displacements opposite to the center and recirculation at the corners. This has led to expansive strains close to the center of trough (red color in Fig. 3c), compressive strains near the side edges (blue), and strains close to zero in between. The exact shape of the inhomogeneous deformation field will likely depend on the interactions, or "stickiness", between the CNT layer and the trough walls. The asymmetry along the centerline is probably a result of the heterogeneous distribution of CNTs at the interface. This is the first time such a complex flow field is captured experimentally. Shear strain (ε_{xy}) was calculated to be on the order of 0.12, one order of magnitude smaller than ε_{xx} at large compression. Shear strain data are included in Supporting Information (Fig. S4).

Mapping out the global strain field during an actual LP trough experiment allows us to further quantitatively assess the validity of a 1D uniaxial compression assumption. The strain at the center of the trough was calculated by averaging the strain inside an imaginary Wilhelmy plate as represented by a black rectangle at the trough center in Fig. 3c. The imaginary plate has the same dimensions (19.62 mm × 0.5 mm) as the actual plates used experimentally. Strain components, ε_{xx} and ε_{yy}, were calculated by assuming the plate oriented parallel and perpendicular to the barriers, respectively, as in actual surface stress measurements. Fig. 4a shows the local ε_{xx} and ε_{yy} values obtained from DIC analysis (i.e., $\varepsilon_{xx,DIC}$ and $\varepsilon_{yy,DIC}$) and the strain calculated by assuming 1D uniaxial compression ($\varepsilon_{xx,1D}$). The uniaxial compression assumption underestimates the magnitude of the strain at large compression. For instance, $\varepsilon_{xx,1D}$ is about 36% smaller than $\varepsilon_{xx,DIC}$ at a compression area of 28 cm^2. ε_{yy} is not defined in the case of 1D uniaxial compression. In DIC analysis, $\varepsilon_{yy,DIC}$ is positive due to the expansive nature close to the center of the trough. The magnitude of $\varepsilon_{yy,DIC}$ increases as a function of increasing compression and reaches a plateau value of 0.28, which coincides with the onset of the "wrinkling" of the CNT layer (shaded area in Fig. 4a). Wrinkling has been observed for interfaces laden with CNT, graphene oxide, and silica particles [5,7,15] as additional area is created at large compressions to accommodate the particles. The surface compressional modulus may be calculated from the wavelength of these wrinkles [16,17] for homogeneous systems, which is not the case for CNTs [5].

Fig. 4b compares the magnitude of the strain ($\varepsilon_{xx,DIC}$) along with that transverse ($\varepsilon_{yy,DIC}$) to the compression direction. The ratio ($\nu = -\varepsilon_{yy,DIC}/\varepsilon_{xx,DIC}$) is analogous to Poisson's ratio which describes a bulk material's resistance to distort under mechanical load versus a volume change [18]. ν equals to 0.5 for a perfectly incompressible material. At small compressions, the ν value for the CNT layer is around 0.4, indicating the compressibility of the CNT layer. Interestingly, further compression results in a decrease in ν. No CNTs were detected in the sub-phase water based on UV absorbance. There are two possible explanations. First, the decrease is caused by the loss of CNTs from the interface due to aggregation, where the CNTs stacked up and escaped the interface [5]. Second, the geometric constraint imposed by the side edges of the trough prevents CNTs from moving further towards the edges at large compressions.

Fig. 4c shows the surface stresses as a function of $\varepsilon_{xx,1D}$, assuming uniaxial compression. The local slope of a stress–strain curve is related to the apparent modulus, or stiffness, of the CNT layer for a given compression area. The steeper the slope, the higher is the modulus. The modulus increases probably due to the compaction of the CNT-laden layer. At large compression (<35 cm^2), the slope of the stress-strain curve decreases slightly as the CNT-layer wrinkles. Fig. 4d shows the surface stresses as a function of DIC-corrected strains ($\varepsilon_{xx,DIC}$). It should be noted that the apparent modulus contains both dilatational and shear components. Following the procedure proposed by Petkov and Gurkov [9], the total surface normal stresses (σ_{xx} and σ_{yy}) were measured in separate experiments using a Wilhelmy plate oriented parallel and perpendicular to the barriers, respectively. Surface pressure data are included in Supporting Information (Fig. S5). The evolution of surface pressure and its relation to CNT microstructure have been analyzed and discussed in detail in a previous paper [5]. For a viscoelastic surface:

$$\begin{aligned} \tau_{xx} &= (K + G)\varepsilon_{xx} + (K - G)\varepsilon_{yy} + (\mu + \eta)D_{xx} + (\mu - \eta)D_{yy} \\ \tau_{yy} &= (K - G)\varepsilon_{xx} + (K + G)\varepsilon_{yy} + (\mu - \eta)D_{xx} + (\mu + \eta)D_{yy} \end{aligned} \quad (3)$$

where τ_{xx} is the extra surface stresses (i.e., $\tau_{xx} = \sigma_{xx} - \sigma_{eq}$, where σ_{eq} is the equilibrium value in the non-deformed state) along the compression direction, τ_{yy} is the extra surface stresses perpendicular to the compression, K is the surface dilatational modulus, G is the surface shear modulus, μ is the surface dilatational viscosity, η is the surface shear viscosity, ε_{xx} is the strain along the compression direction, ε_{yy} is the strain perpendicular to the compression direction, D_{xx} is the strain-rate along the compression direction, and D_{yy} is the strain-rate perpendicular to the compression direction.

The effect of compression rate and corresponding relaxation behavior of CNT layers will be explored and reported in a future paper as they are beyond the scope of this study, which focuses on putting forward an experimental technique for global strain field mapping. For simplicity, it is also assumed that the compression rate is sufficiently high, relative to the characteristic relaxation time of the CNT layer, such that the response is primarily elastic with negligible viscous contribution. It is worth noting that the DIC analysis is based on tracking the movement of CNT speckle

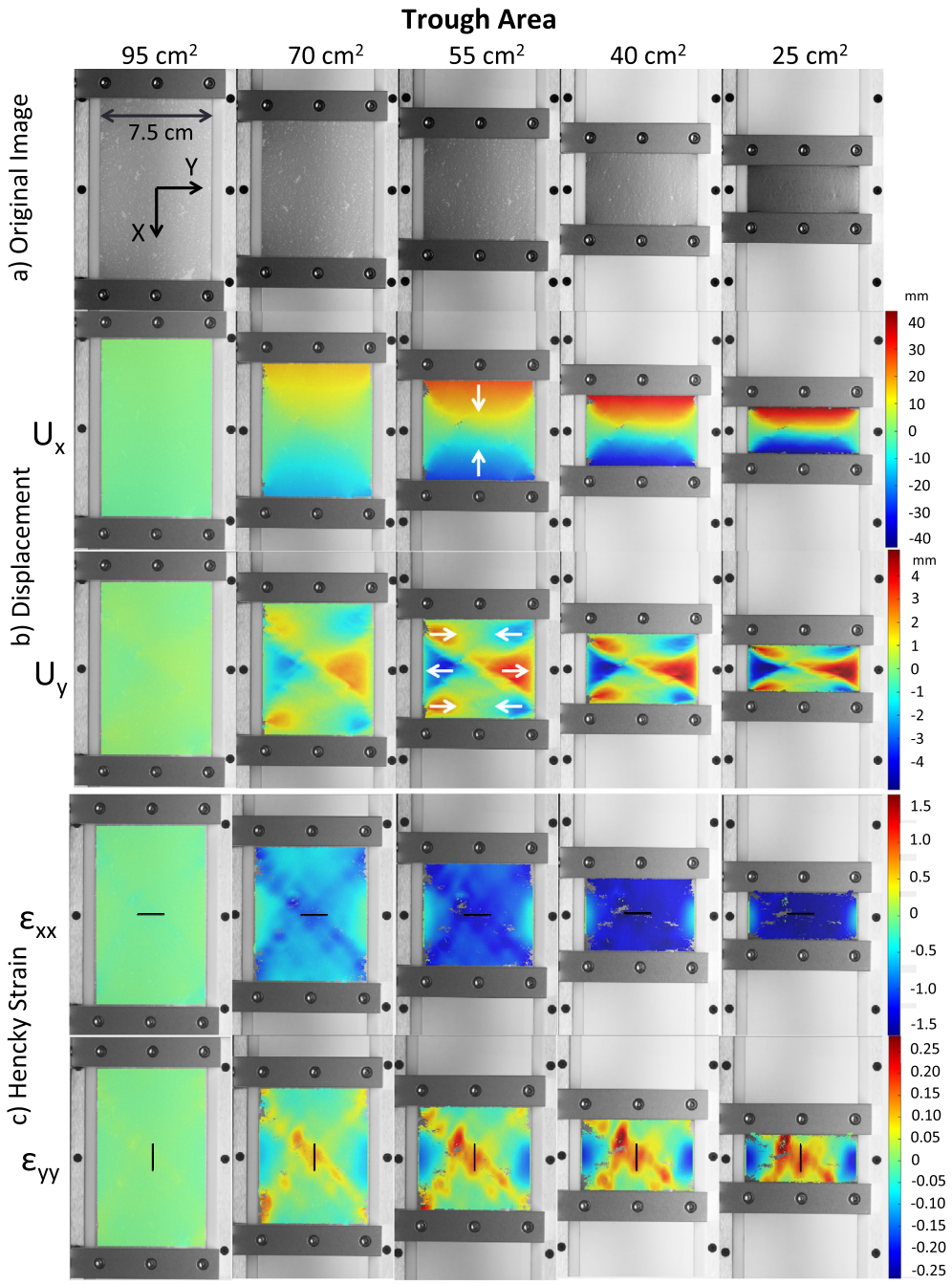

Fig. 3. (a) A series of original images captured using the experimental setup shown in Fig. 1. (b) and (c) show the displacements (with respect to the first image) and Hencky strains calculated form these images using DIC analysis (Ncorr). The black rectangle at the centre of each image indicates the position of the imaginary Wilhelmy plate for calculating the local strain. CNT amount = 0.684 mg; compression rate = 5 mm/min; r_s = 60 pixels, S = 12 pixels, and r_{st} = 10 pixels.

pattern, which is prone to relaxation of the CNT layer. The slower the compression rate, the more time the CNT layer will be allowed to relax. Two compression rates were used to explore the effect of compression rate on the DIC results. As the compression rate was decreased from 5 mm/min to 1 mm/min, the strain field approaches the 1D uniaxial compression assumption (Fig. S6). In the original work by Petkov and Gurkov, only the first terms on the right hand side of the equations remain for 1D uniaxial compression. In the DIC-corrected cases, both ε_{xx} and ε_{yy} are defined and known. K and G values were calculated for both the 1D uniaxial compression case and the 2D DIC-corrected case. Fig. 4e and f show K and G as a function of strain for the 1D uniaxial compression (K_{1D}, G_{1D}) and the DIC-corrected case (K_{DIC}, G_{DIC}), respectively. In both cases, the dilatational modulus (K) first increases as the CNT layer are compressed and then reaches a maximum before the onset of the wrinkling transition. However, K_{1D} reaches a maximum value of around 70 mN/m, as opposed to K_{DIC} that reaches a maximum value of 62 mN/m. The difference is attributed to the underestimation of strain in the 1D uniaxial compression case. The surface shear modulus (G) is similar for both cases, showing slight strain-softening behavior at higher strains.

To compare the overall DIC-corrected strain with the 1D uniaxial strain for a given compression area, the average strain along the direction of compression ($\bar{\varepsilon}_{xx,DIC}$) and that transverse to the

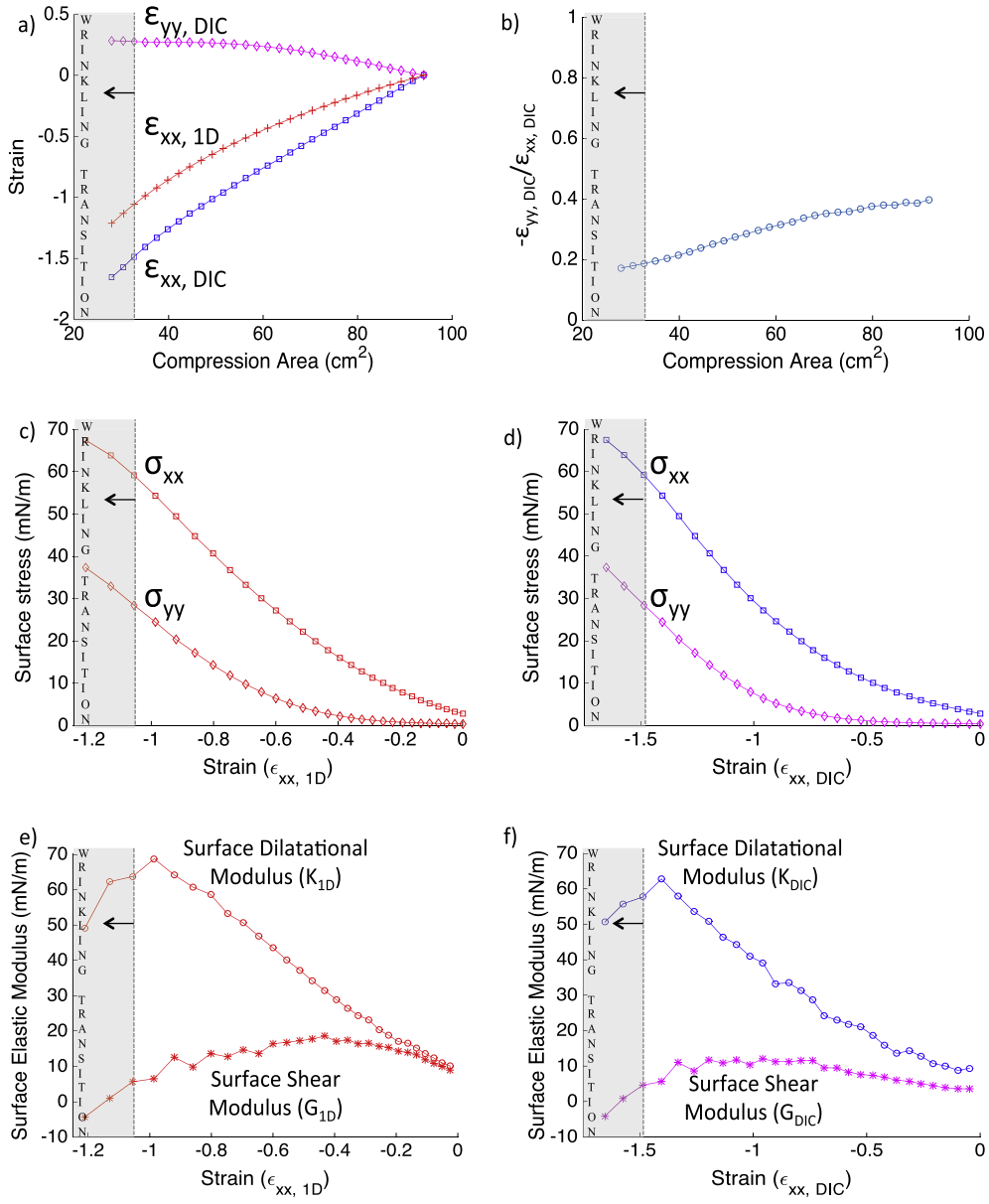

Fig. 4. (a) DIC-corrected strains ($\varepsilon_{xx,DIC}$ and $\varepsilon_{yy,DIC}$) versus strains calculated by assuming uniaxial compression ($\varepsilon_{xx,1D}$) as a function of compression area. (b) The ratio between DIC-computed strains along and perpendicular to the compression direction. Surface stresses as a function of: (c) $\varepsilon_{xx,1D}$ and (d) $\varepsilon_{xx,DIC}$. Surface dilatational (K) and shear (G) moduli as a function of: (e) $\varepsilon_{xx,1D}$ and (f) $\varepsilon_{xx,DIC}$.

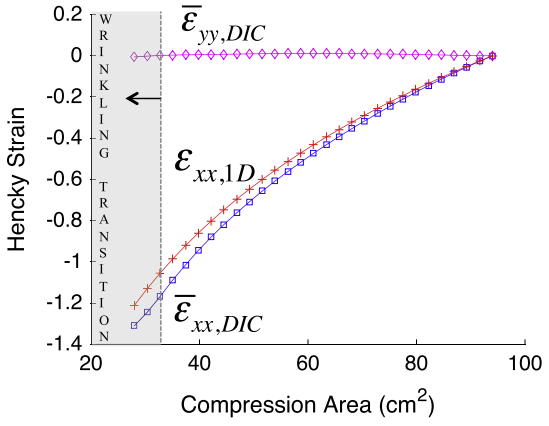

Fig. 5. Average DIC corrected strains ($\bar{\varepsilon}_{xx,DIC}$ and $\bar{\varepsilon}_{yy,DIC}$) and 1D uniaxial strain ($\varepsilon_{xx,1D}$) as a function of compression area.

compression direction ($\bar{\varepsilon}_{yy,DIC}$) were calculated by averaging all the local strains within the open trough area. Fig. 5 shows that the average DIC-corrected values closely resembles the 1D uniaxial strain values $\bar{\varepsilon}_{xx,DIC}$, whereas the $\bar{\varepsilon}_{yy,DIC}$ values remain close to zero, further supporting the use of the DIC correction method.

3.2. Sensitivity analysis and limitations

In the DIC analysis, three parameters, namely, r_s, S, and r_{st}, were specified by the user. These parameters are defined in the DIC protocol section and Fig. 2. Sensitivity analysis was carried out to understand how these parameters may affect the calculated strain. Fig. 6a and b show the variation in the calculated values of $\varepsilon_{xx,DIC}$ and $\varepsilon_{yy,DIC}$ as a function of percent change in r_s, S, and r_{st}. The results suggest calculated strains are rather insensitive to the exact values of S and r_{st} used in DIC analysis, which were arbitrarily chosen to be 12 pixels and 10 pixels, respectively. The largest change

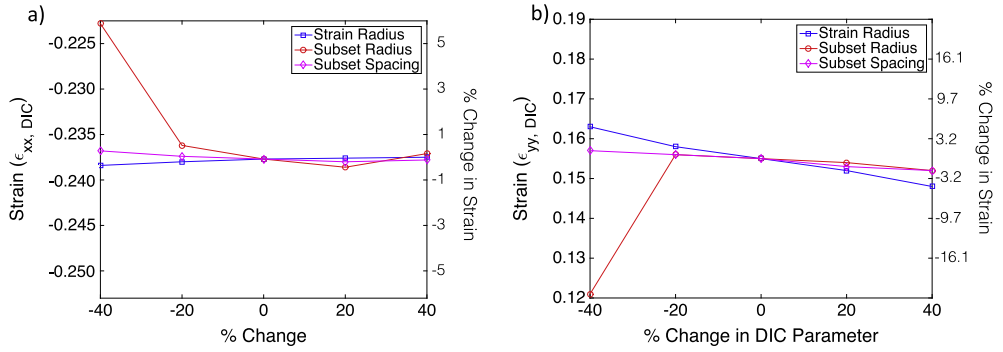

Fig. 6. Sensitivity analysis of three user-defined parameters (namely, subset radius, subset spacing, and strain radius) used in DIC analysis. The reference (zero-percent change) values of r_s, S, and r_{st} are 60 pixels, 12 pixels and 10 pixels, respectively.

in the calculated strains ($\varepsilon_{xx,DIC}$ and $\varepsilon_{yy,DIC}$) was observed when the r_s is 40% smaller than the arbitrarily chosen value of 60 pixels. This is probably caused by the noise involved in digital imaging.

Despite the robustness of the DIC analysis, the current study has a number of limitations. First, the success of DIC analysis relies on the presence or creation of an appropriate speckle pattern [13]. Second, unlike solid samples used in tensile test, particles or molecules may desorb from the interface during compression, leading to a change in optical texture and failure of the DIC analysis. In this study, the UV absorbance of the sub-phase water was measured to confirm that no CNTs desorbed during compression, which is also consistent with previous findings [5,7]. However, this may not be the case for other interfacial systems. Third, this method cannot correct for the stress field or local strain field modified by the presence of a Wilhelmy plate. The insertion of a Wilhelmy plate creates a meniscus that likely affect the particle distribution close to the plate [19]. In-plane stress measurements, such as microtensiometer [20], may be used in conjunction with the DIC method reported in this paper to alleviate this problem. Finally, dilatational and shear strain decoupling relies on the constitutive model proposed by Petkov and Gurkov, which strictly speaking only applies to linear viscoelastic systems where the moduli are independent of strains. The surface dilatational and shear moduli calculations assume an elastic layer and ignore any viscous dissipation.

4. Summary and conclusions

To summarize, this paper reports a new experimental method of applying digital image correlation (DIC) to a particle-laden interface to map out the complete global strain field. The analysis takes advantage of the intrinsic speckle pattern present in a CNT-laden interface and requires no addition of foreign particles as in previous studies. The strains calculated are rather insensitive to the arbitrarily chosen user-defined parameters (e.g., subset radius, subset spacing, and strain radius) in the DIC analysis. The common 1D uniaxial compression assumption underestimated the local strain at large compression and overestimated the surface elastic moduli. All in all, this work confirms, for the first time, the complexity of the strain field created during a LP trough experiment, while offering a possible way to capture the actual strain field. The technique reported in this paper may be applied to study other insoluble layer systems beyond CNTs. In cases where a speckle pattern is absent, the use of foreign probe particles or a different imaging technique, such as Brewster angle and fluorescence microscopy, may be required. However, cautions must be exercised as the presence of probe particles may modify the intrinsic behavior of interest and the change in optical texture may be too large for DIC to handle. The findings also support the need to develop new experimental tools (e.g., radial trough [21]) to create a simpler deformation field for characterizing the rheological responses of an interface. Further studies will be pursued to: (i) evaluate the applicability of this technique to other material systems, (ii) assess the quality of a speckle pattern quantitatively [22], and (iii) investigate the effects of desorption [23], 3D aggregation [5], and wrinkling [11,16,17] on the DIC strain analysis.

Acknowledgment

We thank Professor H. Henning Winter (UMass Amherst) and Professor Jan Vermant (ETH Zurich) for helpful discussions. This material is based upon work supported by the U.S. National Science Foundation CAREER award under Grant No. 1253613. S.R. Vora would also like to acknowledge GE Graduate Fellowship and Anton Paar Research Fellowship for financial support.

Appendix A. Supplementary material

Supplementary data associated with this article can be found, in the online version, at http://dx.doi.org/10.1016/j.jcis.2017.08.082.

References

[1] A. Pockels, On the relative contamination of the water-surface by equal quantities of different substances, Nature 46 (1192) (1892) 418–419.
[2] G.G. Fuller, J. Vermant, Editorial: dynamics and rheology of complex fluid–fluid interfaces, Soft Matter 7 (17) (2011) 7583.
[3] G.G. Fuller, J. Vermant, Complex fluid-fluid interfaces: rheology and structure, Annu. Rev. Chem. Biomol. Eng. 3 (2012) 519–543.
[4] D.A. Edwards, H. Brenner, D.T. Wasan, Interfacial Transport Processes and Rheology, Butterworth-Heinemann, 1991.
[5] S.R. Vora, B. Bognet, H.S. Patanwala, F. Chinesta, A.W.K. Ma, Surface pressure and microstructure of carbon nanotubes at an air-water interface, Langmuir 31 (16) (2015) 4663–4672.
[6] V.B. Fainerman, V.I. Kovalchuk, E.H. Lucassen-Reynders, D.O. Grigoriev, J.K. Ferri, M.E. Leser, M. Michel, R. Miller, H. Möhwald, Surface-pressure isotherms of monolayers formed by microsize and nanosize particles, Langmuir 22 (4) (2006) 1701–1705.
[7] L. Imperiali, K.-H. Liao, C. Clasen, J. Fransaer, C.W. Macosko, J. Vermant, Interfacial rheology and structure of tiled graphene oxide sheets, Langmuir 28 (21) (2012) 7990–8000.
[8] T. Verwijlen, L. Imperiali, J. Vermant, Separating viscoelastic and compressibility contributions in pressure-area isotherm measurements, Adv. Colloid Interface Sci. 206 (2014) 428–436.
[9] J.T. Petkov, T.D. Gurkov, B.E. Campbell, R.P. Borwankar, Dilatational and shear elasticity of gel-like protein layers on air/water interface, Langmuir 16 (8) (2000) 3703–3711.
[10] B.R. Malcolm, The powder method for the study of condensed langmuir monolayers with applications to polymers, Langmuir 11 (1) (1995) 204–210.
[11] E. Aumaitre, D. Vella, P. Cicuta, On the measurement of the surface pressure in langmuir films with finite shear elasticity, Soft Matter 7 (6) (2011) 2530.
[12] S. Osswald, M. Havel, Y. Gogotsi, Monitoring oxidation of multiwalled carbon nanotubes by raman spectroscopy, J. Raman Spectrosc. 38 (6) (2007) 728–736.
[13] B. Pan, K. Qian, H. Xie, A. Asundi, Two-dimensional digital image correlation for in-plane displacement and strain measurement: a review, Meas. Sci. Technol. 20 (6) (2009) 62001.

[14] J. Blaber, B.S. Adair, A. Antoniou, Ncorr: open-source 2D DIC matlab software, Exp. Mech. 55 (6) (2015) 1105–1122.
[15] D.Y. Zang, E. Rio, D. Langevin, B. Wei, B.P. Binks, Viscoelastic properties of silica nanoparticle monolayers at the air-water interface, Eur. Phys. J. E. Soft Matter 31 (2) (2010) 125–134.
[16] K.D. Danov, P.A. Kralchevsky, S.D. Stoyanov, Elastic langmuir layers and membranes subjected to unidirectional compression: wrinkling and collapse, Langmuir 26 (1) (2010) 143–155.
[17] D. Vella, P. Aussillous, L. Mahadevan, Elasticity of an interfacial particle raft, Europhys. Lett. 68 (2) (2004) 7.
[18] G.N. Greaves, A.L. Greer, R.S. Lakes, T. Rouxel, Poisson's ratio and modern materials, Nat Mater 10 (11) (2011) 823–837.
[19] L. Botto, E.P. Lewandowski, M. Cavallaro, K.J. Stebe, capillary interactions between anisotropic particles, Soft Matter 8 (39) (2012) 9957.
[20] P. Gijsenbergh, M. Pepicelli, C.L. Wirth, J. Vermant, R. Puers, Langmuir monolayer characterization via polymer microtensiometers, Sens. Actuat. A Phys. 229 (2015) 110–117.
[21] T.M. Bohanon, J.M. Mikrut, B.M. Abraham, J.B. Ketterson, S. Jacobson, L.S. Flosenzier, J.M. Torkelson, P. Dutta, Apparatus with an elastic barrier for radial compression of liquid supported monolayers, Rev. Sci. Instrum. 63 (2) (1992) 1822–1825.
[22] D. Lecompte, A. Smits, S. Bossuyt, H. Sol, J. Vantomme, D. Van Hemelrijck, A.M. Habraken, Quality assessment of speckle patterns for digital image correlation, Opt. Lasers Eng. 44 (11) (2006) 1132–1145.
[23] M. Basavaraj, G. Fuller, J. Fransaer, J. Vermant, Packing, flipping, and buckling transitions in compressed monolayers of ellipsoidal latex particles, Langmuir 22 (15) (2006) 6605–6612.